Three-qubit parity gate via simultaneous cross-resonance drives

Toshinari Itoko,[1,*] Moein Malekakhlagh,[2] Naoki Kanazawa,[1] and Maika Takita[2]

[1] *IBM Quantum, IBM Research–Tokyo, Tokyo, Japan*

[2] *IBM Quantum, IBM Thomas J. Watson Research Center, Yorktown Heights, New York 10598, USA*

(Received 28 September 2023; revised 25 January 2024; accepted 31 January 2024; published 11 March 2024)

Native multiqubit parity gates have various potential quantum computing applications, such as entanglement creation, logical state encoding, and parity measurement in quantum error correction. Here, using simultaneous cross-resonance drives on two control qubits with a common target, we demonstrate an efficient implementation of a three-qubit parity gate. We have developed a calibration procedure based on that for the echoed cross-resonance gate. We confirm that our use of simultaneous drives leads to higher interleaved randomized benchmarking fidelities than a naive implementation with two consecutive controlled NOT gates. We also demonstrate that our simultaneous parity gates can significantly improve the parity measurement error probability for the heavy-hexagon code on an IBM Quantum processor using seven superconducting qubits with all-microwave control.

DOI: 10.1103/PhysRevApplied.21.034018

I. INTRODUCTION

Standard implementation of quantum computing [1,2] involves expressing multiqubit operations in terms of a universal set of single- and two-qubit gates [3]. Through quantum circuit optimization, one can achieve an equivalent shallower-depth circuit, benefiting not only from less incoherent error, caused by energy relaxation and dephasing [4–6], but also possibly from less coherent (control) error. At a high level, strategies for circuit optimization can be software-inspired [7–11] and/or hardware-inspired [12–20]. The former employs unitary group identities for simplification, while the latter considers the hardware connectivity, and explores the hardware potential to achieve more efficient two-qubit or multiqubit gates. Here, following the latter approach, and inspired by cross-resonance (CR) [21–25] quantum processors provided by IBM, we study a three-qubit parity (TP) gate [26], and provide an efficient calibration based on the existing echoed cross-resonance (ECR) scheme [25,27–30].

Having efficient parity gates [31,32] in the native gate set is useful for numerous applications. In particular, the utility of a TP gate boils down to its local equivalence with two consecutive controlled NOT (CNOT) gates (two-CX) on three qubits, in which they share either a common control (or target) qubit [Fig. 1(a)]. Such a circuit subroutine appears for instance in (i) the creation of multiqubit entanglement, in particular the Greenberger-Horne-Zeilinger state [33,34], (ii) logical encoder and parity check syndrome measurement in quantum error correction (QEC) [35–37], and (iii) successive swaps across a qubit network [38,39].

In this paper, we present a TP gate implementation that fits well with IBM's CR architecture. Our implementation closely follows that of the ECR gate [25,28–30], but instead employs two simultaneous CR drives with a common target qubit, hence named simultaneous cross-resonance parity (SCRP) gate [Figs. 1(b) and 1(c)]. This protocol implements a three-qubit Z-parity gate, which is locally equivalent to any other TP gates. Our use of simultaneous drives should work in principle if each CR pulse leads only to a ZX interaction between the intended qubits. In other words, SCRP gives ZXI and IXZ interactions [40], which are commutative, hence additive. Intuitively, the SCRP implementation should improve the fidelity of the Z-parity gate mainly due to its shorter pulse schedule. We confirm that unwanted cross-drive contributions are indeed higher-order effects, and hence weaker, by deriving an effective three-qubit gate Hamiltonian using Schrieffer-Wolff perturbation theory (SWPT) [25,41–45] (Sec. II). Using interleaved randomized benchmarking (IRB) [46], we demonstrate improved error per gate (EPG) for the SCRP implementation compared to two-CX. Furthermore, we demonstrate that the SCRP implementation improves the fidelity of parity measurement on an IBM Quantum processor [47], namely `ibm_auckland`. In particular, the SCRP implementation can reduce the average syndrome error probability of X-parity measurement for the heavy-hexagon code [48–50] compared with a naive implementation with CNOT gates on the device (Sec. IV).

The rest of this paper is organized as follows. First, in Sec. II, we study effective gate interactions for the SCRP

*itoko@jp.ibm.com

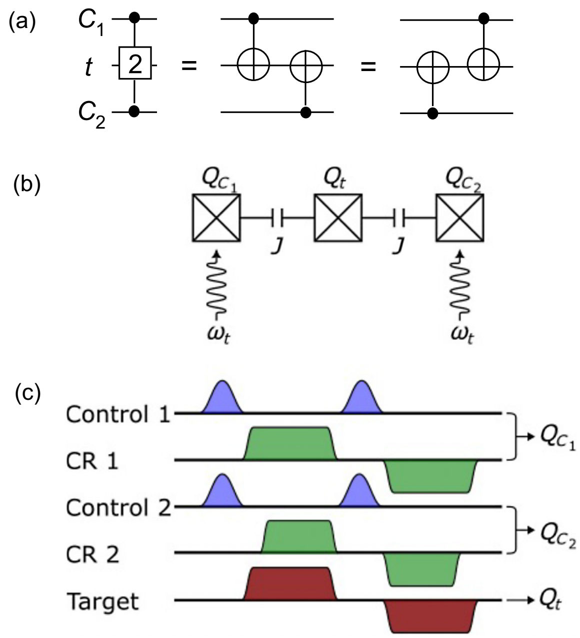

FIG. 1. Implementation of a three-qubit parity gate with simultaneous CR drives. (a) Circuit representation of a Z-parity gate, equivalent to two consecutive CNOT gates with a common target. The case with a common control is locally equivalent up to single-qubit Hadamard gates. (b) Cross-resonance schematics with two control (c_1 and c_2) and one target (t) qubits. (c) Pulse-level implementation using simultaneous echoed CR drives. Each of the two pairs of X_π pulses (blue) have a carrier frequency resonant with the respective control qubit. The CR (green) and rotary (red) pulses have a carrier frequency resonant with the target qubit.

gate implementation using SWPT. In Sec. III, we discuss the SCRP calibration of the TP gate, and provide IRB results that demonstrate improvement in EPG with respect to the standard two-CX implementation. Furthermore, in Sec. IV, we showcase the SCRP gate's utility in improving the syndrome measurement success probability of the heavy-hexagon code. Finally, Sec. V concludes the paper, and examines further potential applications and extensions of the SCRP idea.

II. HAMILTONIAN ANALYSIS

We next provide a Hamiltonian analysis for the SCRP gate, based on SWPT [24,25,43]. Our analysis clarifies why the SCRP gate works in practice: at sufficiently weak CR drive, the effective ZXI and IXZ rates depend only on their corresponding drive amplitudes. Furthermore, undesired three-qubit cross interactions such as the ZXZ and ZIZ terms appear only at higher order, and hence are weaker.

We model the transmon qubits as a set of Duffing oscillators with nearest-neighbor exchange interaction under the rotating-wave approximation as

$$\hat{H}_s = \sum_{j=c_1,c_2,t}\left(\omega_j \hat{a}_j^\dagger \hat{a}_j + \frac{\alpha_j}{2}\hat{a}_j^\dagger\hat{a}_j^\dagger\hat{a}_j\hat{a}_j\right) + \sum_{\langle j,k\rangle} J_{jk}\left(\hat{a}_j^\dagger \hat{a}_k + \hat{a}_j\hat{a}_k^\dagger\right), \tag{1}$$

with ω_j, α_j, and J_{jk} as the qubit frequency, anharmonicity, and pairwise exchange interaction, respectively, for $j,k \in \{c_1, c_2, t\}$. Furthermore, we model the CR and a possible direct target drives as

$$\hat{H}_d(t) = \sum_{j=c_1,c_2,t}\frac{1}{2}\left[\Omega_j^*(t)e^{i\omega_d t}\hat{a}_j + \Omega_j(t)e^{-i\omega_d t}\hat{a}_j^\dagger\right], \tag{2}$$

with $\Omega_j(t) \equiv \Omega_{jX}(t) + i\Omega_{jY}(t)$ and ω_d denoting the complex-valued envelope and the common carrier frequency, respectively. In the rotating frame (RF) of the drive, which is set to the target qubit frequency, the Hamiltonian simplifies to

$$\hat{H}_{\rm rf}(t) \equiv \sum_{j=c_1,c_2,t}\left(\Delta_{jd}\hat{a}_j^\dagger\hat{a}_j + \frac{\alpha_j}{2}\hat{a}_j^\dagger\hat{a}_j^\dagger\hat{a}_j\hat{a}_j\right) + \sum_{\langle j,k\rangle} J_{jk}\left(\hat{a}_j^\dagger\hat{a}_k + \hat{a}_j\hat{a}_k^\dagger\right) + \sum_{j=c_1,c_2,t}\frac{1}{2}\left[\Omega_j^*(t)\hat{a}_j + \Omega_j(t)\hat{a}_j^\dagger\right], \tag{3}$$

where $\Delta_{jd} \equiv \omega_j - \omega_d$. The RF Hamiltonian (3) is the starting point of our analysis. To understand the SCRP power budget, for simplicity, we assume an always-on X-quadrature-only continuous-wave drive $\Omega_j(t) = \Omega_j$.

Applying time-independent SWPT, we derive effective (resonant) interactions for the SCRP gate through recursive frame transformations that average over off-resonant transitions [24,25,43] (Appendix A). The relevant SCRP frame is diagonal with respect to the two control qubits, i.e., allowing only I and Z on the controls, and off-diagonal with respect to the target. We treat the first two lines of Eq. (3) as the bare Hamiltonian and the last line as the interaction Hamiltonian.

Up to the zeroth order, the exchange interaction leads to nearest-neighbor static ZZ interactions:

$$\omega_{ZZI}^{(0)} = \frac{J_{c_1t}^2}{\Delta_{c_1t} - \alpha_t} - \frac{J_{c_1t}^2}{\Delta_{c_1t} + \alpha_{c_1}}, \tag{4}$$

$$\omega_{IZZ}^{(0)} = \frac{J_{c_2t}^2}{\Delta_{c_2t} - \alpha_{c_2}} - \frac{J_{c_2t}^2}{\Delta_{c_2t} + \alpha_{c_2}}. \tag{5}$$

Up to the dominant (linear) order in drive amplitudes, the ZXI and IXZ terms are independent, i.e., no cross-drive exists, justifying why such a simultaneous calibration works:

$$\omega_{ZXI}^{(1)} = -\frac{J_{c_1t}\alpha_{c_1}}{\Delta_{c_1t}(\Delta_{c_1t}+\alpha_{c_1})}\Omega_{c_1}, \quad (6)$$

$$\omega_{IXZ}^{(1)} = -\frac{J_{c_2t}\alpha_{c_2}}{\Delta_{c_2t}(\Delta_{c_2t}+\alpha_{c_2})}\Omega_{c_2}, \quad (7)$$

$$\omega_{IXI}^{(1)} = \Omega_t - \frac{J_{c_1t}}{\Delta_{c_1t}+\alpha_{c_1}}\Omega_{c_1} - \frac{J_{c_2t}}{\Delta_{c_2t}+\alpha_{c_2}}\Omega_{c_2}. \quad (8)$$

At second and higher order in drive amplitudes, we find weak cross-drive contributions which can be categorized as: (i) renormalization of the original CR interactions in each two-qubit subspace (such as Stark shifts, *ZZI* and *IZZ* rates, as well as the desired *ZXI*, *IXZ* terms) due to the other CR drive, and (ii) emergence of new interactions such as *ZXZ* and *ZIZ* terms that couple the two control qubits. Our analysis shows that both categories tend to be reasonably weak (O(1–10) kHz) (see Appendix A).

Based on Eqs. (6) and (7), the cross-drive-free nature of the desired *ZXI* and *IXZ* rates up to the leading order allows us to employ the existing CR echo calibration [25,27–30] in constructing the SCRP gate. In particular, the CR echo sequence removes the *IXI* term, and suppresses the dominant error terms *ZZI* and *IZZ* up to the leading order. We discuss the SCRP calibration in more detail in the following section.

III. PARITY GATE CALIBRATION

Our SCRP pulse schedule for implementing a three-qubit Z-parity gate is shown in Fig. 1(c), which is inspired by the CR echo calibration for the CNOT gate [27,28]. The main part (green) consists of two echoed sequences of simultaneous CR drives onto the control qubits c_1 and c_2 with the carrier frequencies set to the target qubit frequency. Moreover, interleaving X_π pulses (blue) onto the control qubits c_1 and c_2 allows for echoing out nearest-neighbor *ZZ* (i.e., *ZZI* and *IZZ*), as well as the *IXI* Hamiltonian terms up to the leading order [25,30]. Each individual CR echo calibration may also be accompanied with simultaneous resonant rotary tones onto the target qubit t (shown altogether in red) [30]. The rotary tones were designed to suppress several unwanted terms in the effective Hamiltonian of the echoed CR drives, namely the Y error on the target as well as target-spectator crosstalk [30]. We used the default pulse shapes provided by IBM Quantum systems, which are Gaussian with the derivative removal by adiabatic gate (DRAG) [51] for X_π pulses, and square Gaussian (square with Gaussian ramps) for CR and rotary pulses. To implement a Z-parity gate, three additional local Clifford instructions are needed in front (or back) of the schedule, namely $Z_{\pi/2}$ on c_1 and c_2, and X_π on t.

We have developed a straightforward calibration procedure for the Z-parity gate based on the well-established CR echo calibration for CNOT gates [27,28], where we adopt the two CR echo pulse configurations, i.e., amplitudes and angles, while we replace the independently calibrated rotary tones with a newly calibrated single rotary tone. For example, to implement a Z-parity gate on qubits (0, 1, 2), we use pulse amplitudes and angles calibrated for CR(0, 1) and CR(2, 1) as those for two echoed CR pulses to drive simultaneously. We place two echoed CR sequences so that their X_π pulses in center are aligned as shown in Fig. 1(c). Note that we could recalibrate those CR pulses at once so that they have the same duration and the resulting rotation in the target qubit becomes the desired angle for any binary input to the two control qubits, i.e., π for 00, $-\pi$ for 11, and 0 for 01 and 10. However, our preliminary experiments suggest the improvement by such an extra calibration should be marginal or negligible. Therefore, for simplicity, we reuse CR pulse configurations for two-qubit gates to implement SCRP gates in all experiments we conduct hereafter. To calibrate the simultaneous rotary tone in our SCRP implementation, we adopt and generalize the Hamiltonian error amplifying tomography (HEAT) technique [30] (see Appendix B).

We characterize the potential improvement by the SCRP implementation in the fidelity of a Z-parity gate by comparing it with a naive implementation with two consecutive CNOT gates using IRB [46]. We prepare two interleaved sequences from a common reference Clifford sequence. Both interleave a Z-parity gate, but with different implementations: one implemented with SCRP and the other implemented with two CNOT gates (see Appendix C). We conducted such an IRB experiment using qubits (8, 11, 14) on `ibm_auckland`. We used ten Clifford lengths: 2, 3, 4, 5, 7, 9, 12, 17, 25, and 38. For each Clifford length, we sampled 50 randomized benchmarking (RB) circuits and computed survival rate from 400 shots for each circuit. We fit an exponential curve to the averaged survival rates (over the IRB seeds and shots) [46].

Figure 2 shows the result obtained from the IRB experiment. It contains three decay curves corresponding to a reference sequence (blue), interleaved SCRP implementation (green), and interleaved two-CX implementation (orange) of the Z-parity gate, respectively. The decay curve of SCRP appears clearly higher than that of two-CX, suggesting a higher gate fidelity. For reference, the EPG estimated by the ratio of decay rates (the reference and the sequence of interest) was improved from 0.02109 ± 0.00105 (two-CX) to 0.00964 ± 0.00095 (SCRP). This improvement is in part due to the reduction in the gate length from 704.0 ns (two-CX) to 369.8 ns (SCRP). Estimating the best possible average gate error based on the coherence limit [52,53], we find the limits as 0.0122 (two-CX) and 0.00645 (SCRP). These coherence limits are calculated from the gate lengths, T_1 values of $(122.7, 134.8, 159.7)$ µs, and T_2 values of (73.4, 111.4, 170.3) µs, for `ibm_auckland` qubits (8, 11, 14), respectively (see Appendix D).

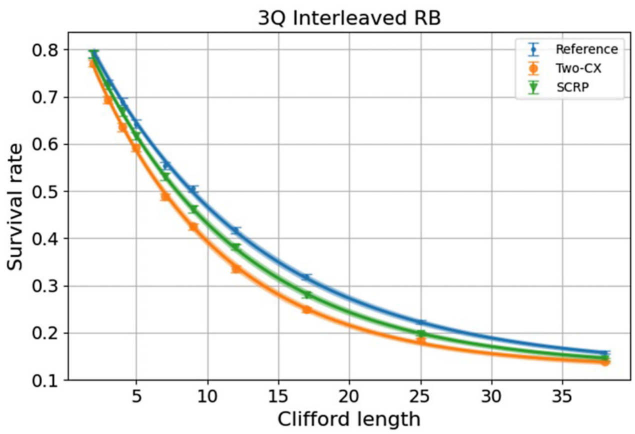

FIG. 2. IRB comparing two Z-parity gate implementations: consecutive two CNOT gates (two-CX, orange) and simultaneous CR drives (SCRP, green) on qubits (8, 11, 14) on `ibm_auckland`. Each point represents the average survival rate over 50 sequences for a Clifford length (each error bar indicates the standard deviation of the average) and solid curves represent the fitting curves (their thickness with shaded region indicate 3σ confidence intervals). The estimated EPGs are 0.02109 ± 0.00105 (two-CX) and 0.00964 ± 0.00095 (SCRP).

IV. DEMONSTRATIONS

We next demonstrate how the SCRP calibration improves the fidelity of parity measurement for QEC on IBM devices. Here, we focus on the X-parity measurement of the heavy-hexagon code [48–50]. The circuit realization requires seven qubits, consisting of four data qubits (D1–D4, gray), two flag qubits (F1 and F2, white) and one syndrome qubit (S, black), with a connectivity with degree at most three, as shown in Fig. 3(a). The standard X-parity check circuit is originally represented with eight CNOT gates, as shown in Fig. 3(b). It consists of four pairs of two CNOT gates with a common control and distinct target qubits, i.e., X-parity gates, which are locally equivalent to Z-parity gates up to a change of basis using single-qubit Hadamard gates. Applying the replacement, the X-parity check circuit will have an efficient representation with just four Z-parity gates, as shown in Fig. 3(c). We used the latter circuit representation and compared the (i) two-CX and (ii) SCRP implementations of the Z-parity gates.

The `ibm_auckland` processor has 27 qubits, from which we used qubits (5, 8, 9, 11, 13, 14, 16) ordered as (D1, F1, D2, S, D3, F2, D4). Qubit transition frequencies ($\omega_{01}/2\pi$) of the four data qubits (5, 9, 13, 16) are (4.99282, 5.08839, 5.01678, 4.96965) GHz, the two flag qubits (8, 14) are (5.20360, 5.16698) GHz, and the syndrome qubit 11 is 5.05517 GHz, respectively. The qubit anharmonicities $\alpha/2\pi$ do not vary substantially, and are approximately equal to -340 MHz. See Appendix E for the details of the device parameters.

Following Sec. III, we calibrated the SCRP gates on the three qubit triplets {(5, 8, 9), (8, 11, 14), (13, 14, 16)} found in Fig. 3(c). In advance, we also calibrated CR pulses for qubit pairs (5, 8), (9, 8), (13, 14), (16, 14), for which the default CNOT gates are implemented with CR pulses in the opposite direction. For example, CNOT(5, 8) is implemented with CR(8, 5), i.e., CR drive on qubit 8 within the frame of qubit 5, while CR(5, 8) is necessary to implement SCRP gate on (5, 8, 9).

We initialized the four data qubits using all possible 16 product states ranging from $|++++\rangle$ to $|----\rangle$. Here, $|+\rangle$ and $|-\rangle$ are the eigenstates of the Pauli X operator. For each input state, we ran the parity check circuit 40 000 times. The total durations of the circuits were 2261 ns (two-CX) and 1365 ns (SCRP), excluding the input state preparation and the final measurements.

We quantified how much the use of the SCRP gate improves the accuracy of the parity measurement by comparing the syndrome and the data error probabilities. The syndrome error probability is the probability that an incorrect bit is measured at the syndrome qubit. Here, the correct syndrome is 0 when the number of $+$ in an input state is even, and 1 when odd. The data error probability is the probability that a state different from the input is measured

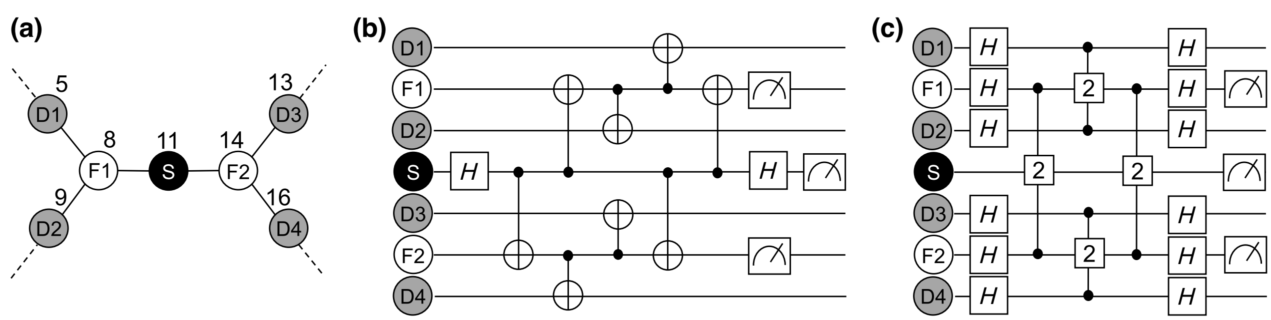

FIG. 3. X-parity measurement circuit for heavy-hexagon code. (a) Seven-qubit subsystem of interest. Nodes represent qubits and edges represent couplers. The numbers on the shoulders of the nodes are the qubit numbers we used on `ibm_auckland`. (b) Original representation with CNOT gates [48]. (c) Representation with Z-parity gates useful for SCRP implementation, which reduces the circuit depth by a factor of approximately 3/5, and uses only four SCRP gates compared to eight CNOT gates.

TABLE I. Syndrome and data error probabilities averaged over 16 initial states of the X-parity measurement. Individual qubit data errors are described in D1–D4 columns.

	Syndrome error (std)	Data error	D1	D2	D3	D4
SCRP	0.088459 (0.001419)	0.095697	0.034948	0.031270	0.017192	0.016798
Two-CX	0.122878 (0.001639)	0.164109	0.045063	0.034634	0.066089	0.030228

at the end of a parity check circuit. Note that those values are affected by state preparation and measurement (SPAM) errors. As shown in Table I, the syndrome error probability averaged over all 16 initial states is significantly improved by the SCRP implementation from 0.1229 down to 0.0885 ($\approx$ 28% improvement), while the average data error rate is reduced from 0.1641 to 0.0957 ($\approx$ 42% improvement).

We conducted the same experiment on different processors and qubits, and confirmed that the SCRP implementation always improves the X-parity measurement regardless of the choice of processors or qubits, with a relative improvement ranging from 9% to 33%. For example, the average syndrome error probability improves from 0.252198 to 0.229439 ($\approx$ 9.0%) on qubits (92, 102, 101, 103, 105, 104, 111) in `ibm_brisbane` and from 0.197723 to 0.131761 ($\approx$ 33%) on qubits (16, 19, 20, 22, 24, 25, 26) in `ibm_sherbrooke` (see Appendix F for more experimental results, including the cases when running circuits with dynamical decoupling sequences).

V. CONCLUSION AND OUTLOOK

We have presented a pulse-level implementation of a Z-parity gate with simultaneous CR drives. We have shown that this SCRP implementation has little unwanted Hamiltonian terms in theory and hence it can achieve better gate fidelity than a naive implementation with CNOT gates in practice. We have also demonstrated using IBM CR devices that our calibrated parity gates significantly improve the error probability of the parity measurement for the heavy-hexagon code. That suggests, as the cost of SCRP gate calibration is not large, optimizing circuits using Z-parity gates can be a good option for reducing errors on superconducting quantum computing devices with all-microwave control.

Although we focused on the X-parity measurement of the heavy-hexagon code in Sec. IV, the Z-parity gate is also naturally useful for the Z-parity measurement. Also, our method for calibrating the Z-parity gate can be extended to four-qubit or more parity gates, which are required for other QEC codes such as the surface code on a square lattice [54–58] or another low-density parity check code on a more dense lattice [59]. Such multiqubit parity gates would also be useful for efficient Hamiltonian simulation, as discussed in Ref. [60]. Scaling our SCRP calibration to more qubits would in principle increase unwanted crosstalk by simultaneous drives on additional control qubits. To mitigate the crosstalk, to begin with, it is essential to have more precise frequency allocation for such higher-degree connectivity lattices. Also, it remains to be seen how effective a single rotary tone on the target qubit is in suppressing crosstalk.

As described in Sec. III, we focused on the echoed sequence for SCRP implementation. Instead, utilizing single (simultaneous) CR pulses could be an alternative SCRP implementation worth investigating in the future. Note that, without echoing, CR pulses may yield non-negligible Z rotation errors on control qubits due to the Stark shift, arising from the off-resonant driving of the control qubits, which requires additional calibration of R_z gates for their suppression, as in the case of CNOT gate implementation [27].

One limitation in the SCRP approach, not mentioned in Sec. IV, is that CR pulses cannot always be calibrated in all pairs of coupled qubits, e.g., due to frequency collisions in physical qubits with fixed frequencies [45,61]. This suggests that, for qubit triplets that are close to frequency collisions, tuning a SCRP gate might not be optimal. However, we expect that improvements in manufacturing process techniques such as laser annealing [62] make our proposal more feasible. Secondly, we have assumed that cross-drive errors in a Z-parity gate with the SCRP implementation is negligible in our pulse-strength regime based on the discussion in Sec. II. This assumption, however, breaks down for faster SCRP gate implementation, which requires stronger drives.

It is worth noting that supporting a parity gate as a native instruction will be useful not only for improving parity measurements but also for optimizing circuits aimed at noisy quantum computers without QEC. For example, circuits with a chain of SWAP gates can be optimized using

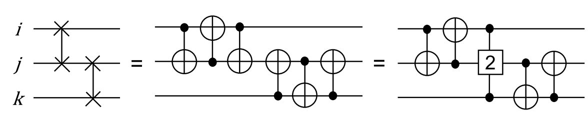

FIG. 4. Optimizing the decomposition of a chain of SWAP gates using Z-parity gates. For $N \geq 2$ successive swaps, standard decomposition requires $3N$ CNOT gates. The Z-parity decomposition, however, requires $(N-1)$ Z-parity, $(N+2)$ CNOT, and $O(2N)$ Hadamard gates. Assuming a similar gate time for the Z-parity and CNOT gates implemented via SCRP and ECR, the decomposition reduces the circuit depth by a factor of approximately 2/3.

Z-parity gates. Such circuits often appear after qubit routing, which transforms a circuit to be executable on a quantum computer with limited qubit connectivity [63–66]. As a SWAP gate is symmetric and SWAP(i,j) is equivalent to CNOT(i,j)–CNOT(j,i)–CNOT(i,j), two consecutive SWAP gates with a common qubit, SWAP(i,j) and SWAP(j,k), can be decomposed into a sequence with a Z-parity gate and four CNOT gates, as shown in Fig. 4. The sequence using a Z-parity gate will have a shorter circuit length than a naive sequence with six CNOT gates, and hence should have a higher fidelity.

ACKNOWLEDGMENTS

The authors thank Luke Govia, David Mackay, Emily Pritchett, and Xuan Wei for helpful discussions and suggestions. We acknowledge the use of IBM Quantum services for this work. The views expressed are those of the authors, and do not reflect the official policy or position of IBM or the IBM Quantum team. For the development of the analytical techniques used to derive the effective gate operation, M.M. acknowledges the support of the Army Research Office under Grant No. W911NF-21-1-0002. The views and conclusions contained in this document are those of the authors and should not be interpreted as representing the official policies, either expressed or implied, of the Army Research Office or the U.S. Government. The U.S. Government is authorized to reproduce and distribute reprints for Government purposes notwithstanding any copyright notation herein.

APPENDIX A: SCHRIEFFER-WOLFF PERTURBATION THEORY

In this appendix, we provide perturbative estimates for the effective Hamiltonian interactions of the SCRP gate via SWPT [25,41–45]. We show that in the sufficiently weak drive limit, and away from frequency collisions [25,45], the SCRP gate exhibits weak cross-CR-drive contributions.

We start from Hamiltonian (3), in the rotating frame of the drive, and partition it into $\hat{H}_{\rm rf}(t) = \hat{H}_0 + \lambda \hat{H}_{\rm int}(t)$, where $\hat{H}_0$ contains the bare qubit and exchange interactions, $\hat{H}_{\rm int}(t)$ includes the two CR-drive contributions, and λ is a bookkeeping parameter. To simplify the perturbation theory, we work in the interaction frame with respect to $\hat{H}_0$ such that $\hat{H}_I(t) \equiv e^{i\hat{H}_0 t}\hat{H}_{\rm int}(t)e^{-i\hat{H}_0 t}$. We then apply a Schrieffer-Wolff (SW) transformation to obtain an effective Hamiltonian as $\hat{H}_{I,\rm eff}(t) \equiv e^{i\hat{G}(t)}[\hat{H}_I(t) - i\partial_t]e^{-i\hat{G}(t)}$, where $\hat{G}(t)$ is the SW generator. Expanding the generator and the effective Hamiltonian in powers of the interaction as $\hat{G}(t) = \sum_{\lambda=1}^{\infty} \lambda^n \hat{G}_n(t)$ and $\hat{H}_{I,\rm eff}(t) = \sum_{\lambda=1}^{\infty} \lambda^n \hat{H}^{(n)}_{I,\rm eff}(t)$, respectively, one arrives at the following set of perturbative SW equations [25,43]:

$$O(\lambda):\quad \begin{cases} \hat{H}^{(1)}_{I,\rm eff} = \mathcal{B}(\hat{H}_I), \\ \dot{\hat{G}}_1 = \mathcal{N}(\hat{H}_I), \end{cases} \tag{A1a}$$

$$O(\lambda^2):\quad \begin{cases} \hat{H}^{(2)}_{I,\rm eff} = \mathcal{B}\left(i[\hat{G}_1, \hat{H}_I] - \frac{i}{2}[\hat{G}_1, \dot{\hat{G}}_1]\right), \\ \dot{\hat{G}}_2 = \mathcal{N}\left(i[\hat{G}_1, \hat{H}_I] - \frac{i}{2}[\hat{G}_1, \dot{\hat{G}}_1]\right), \end{cases} \tag{A1b}$$

$$O(\lambda^3):\quad \begin{cases} \hat{H}^{(3)}_{I,\rm eff} = \mathcal{B}\Big(-\frac{i}{2}[\hat{G}_1, \dot{\hat{G}}_2] - \frac{i}{2}[\hat{G}_2, \dot{\hat{G}}_1] \\ \qquad + \frac{1}{6}[\hat{G}_1, [\hat{G}_1, \dot{\hat{G}}_1]] + i[\hat{G}_2, \hat{H}_I] \\ \qquad - \frac{1}{2}[\hat{G}_1, [\hat{G}_1, \hat{H}_I]]\Big), \\ \dot{\hat{G}}_3 = \mathcal{N}\Big(-\frac{i}{2}[\hat{G}_1, \dot{\hat{G}}_2] - \frac{i}{2}[\hat{G}_2, \dot{\hat{G}}_1] \\ \qquad + \frac{1}{6}[\hat{G}_1, [\hat{G}_1, \dot{\hat{G}}_1]] + i[\hat{G}_2, \hat{H}_I] \\ \qquad - \frac{1}{2}[\hat{G}_1, [\hat{G}_1, \hat{H}_I]]\Big). \end{cases} \tag{A1c}$$

Here $\mathcal{B}(\cdot)$ and $\mathcal{N}(\cdot)$ denote matrix projection onto the effective block-diagonal subspace of the SCRP gate, and the rest, respectively. The effective block-diagonal subspace allows for both diagonal (I or Z) and transverse (X or Y) terms for the target qubit, but only diagonal terms for the control qubits. We keep four levels for each qubit in our perturbative calculation.

Ideally, the CR drive on each control qubit in the SCRP gate should only induce the expected effective CR terms in each subspace, namely IX, ZX, IZ, ZI, and ZZ [24,25,30,43], for which we employ the previously developed ECR calibrations [28,30]. Here, we look closer into deviations from the expected interactions. In particular, we focus on cross-drive contributions that either (i) modify the existing CR terms, or (ii) induce additional control-control interactions.

Up to linear order in the two CR drive amplitudes, one finds the expected CR behavior for each individual two-qubit subspace. The direct exchange interaction between the controls and the shared target causes a fixed ZZ interaction as

$$\omega^{(0)}_{ZZI} = \frac{J^2_{c_1 t}}{\Delta_{c_1 t} - \alpha_t} - \frac{J^2_{c_1 t}}{\Delta_{c_1 t} + \alpha_{c_1}}, \tag{A2}$$

$$\omega^{(0)}_{IZZ} = \frac{J^2_{c_2 t}}{\Delta_{c_2 t} - \alpha_{c_2}} - \frac{J^2_{c_2 t}}{\Delta_{c_2 t} + \alpha_{c_2}}, \tag{A3}$$

obtained up to $O(J^2)$ perturbative diagonalization of $\hat{H}_0$. Furthermore, the dominant effective interactions (linear in CR drive amplitude) are found as

$$\omega_{ZXI}^{(1)} = -\frac{J_{c_1t}\alpha_{c_1}}{\Delta_{c_1t}(\Delta_{c_1t}+\alpha_{c_1})}\Omega_{c_1}, \tag{A4}$$

$$\omega_{IXZ}^{(1)} = -\frac{J_{c_2t}\alpha_{c_2}}{\Delta_{c_2t}(\Delta_{c_2t}+\alpha_{c_2})}\Omega_{c_2}, \tag{A5}$$

$$\omega_{IXI}^{(1)} = \Omega_t - \frac{J_{c_1t}}{\Delta_{c_1t}+\alpha_{c_1}}\Omega_{c_1} - \frac{J_{c_2t}}{\Delta_{c_2t}+\alpha_{c_2}}\Omega_{c_2}. \tag{A6}$$

Based on Eqs. (A4)–(A6), there is no cross-drive contribution in the *ZXI* or *IXZ* terms. The *IXI* term depends on both drive amplitudes. However, this interaction is effectively removed through the echoed CR calibration [28,30].

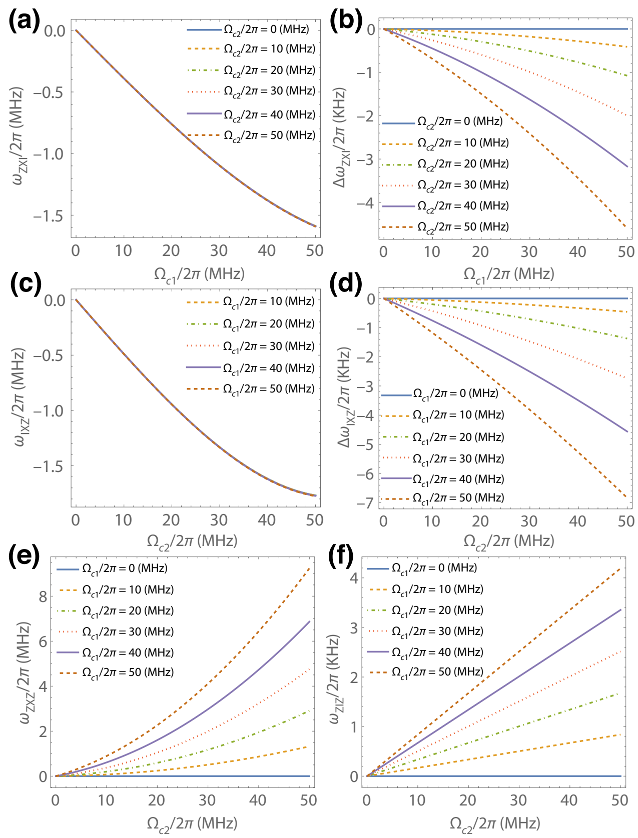

FIG. 5. Examples of cross-drive contributions in the effective three-qubit Hamiltonian, which either modifies the expected two-qubit terms (e.g., *ZXI* and *IXZ*), or leads to new terms involving both control qubits (*ZXZ* and *ZIZ*). (a),(c) The *ZX* term in each subspace as a function of the corresponding control drive, showing weak dependence on the other drive amplitude: (b),(d) cross-drive *ZX* due to the other control drive amplitude; (e) *ZXZ* term; and (f) *ZIZ* term. System parameters are set to $\Delta_{c_1t}/2\pi = 120$, $\Delta_{c_2t}/2\pi = 80$, $J_{c_1t}/2\pi = J_{c_2t}/2\pi = 3$, and $\alpha_{c_1}/2\pi = \alpha_{c_2}/2\pi = \alpha_t/2\pi = -330$ MHz.

Expressions for higher-order terms are quite extensive, and hence not explicitly provided here. We plot example cross-drive contributions in Fig. 5 and discuss the power-law dependence on J, Ω_{c_1}, and Ω_{c_2}. At the second order, one finds large control Stark shifts *ZII* and *IIZ*, corrections to the control-target *IZZ* and *ZZI* terms, as well as a control-control *ZIZ*. These contributions generally scale as $O(\Omega_{c_1}^2)$, $O(\Omega_{c_2}^2)$, $O(J^2\Omega_{c_2}^2)$, $O(J^2\Omega_{c_1}^2)$, and $O(J^2\Omega_{c_1}\Omega_{c_2})$ assuming $J = J_{c_1t} = J_{c_2t}$. Amongst these, the control-control *ZIZ* interaction is *not* addressed by the individual ECR calibrations, and remains as an error term. At the third order, we find $O(J\Omega_{c_1}^3)$, $O(J\Omega_{c_1}^2\Omega_{c_2})$, $O(J\Omega_{c_1}\Omega_{c_2}^2)$, and $O(J\Omega_{c_2}^3)$ contributions to the *IXI*, *ZXI*, *IXZ*, and *ZXZ* terms. Similarly, amongst these, the *ZXZ* term is not addressed by the individual ECR calibrations.

Figure 5 characterizes the cross-drive contribution to the *ZXI*, *IXZ*, *ZXZ*, and *ZIZ* effective terms, for a case with favorable frequency allocation, where the control qubits are 120 and 80 MHz detuned above the target qubit. Panels (a) and (c) show the usual cubic suppression of the *ZXI* and *IXZ* terms at higher power, and very weak dependence on the other control drive amplitude. The weak cross-drive dependence of the *ZXI* rate $\Delta\omega_{ZXI}(\Omega_{c_1},\Omega_{c_2}) \equiv \omega_{ZXI}(\Omega_{c_1},\Omega_{c_2}) - \omega_{ZXI}(\Omega_{c_1},0)$ (similarly for $\Delta\omega_{IXZ}(\Omega_{c_1},\Omega_{c_2})$) are shown in panels (b) and (d), and are found to be $O(1–10)$ kHz. Panels (e) and (f) furthermore characterize the control-control *ZXZ* and *ZIZ* interactions as $O(1–10)$ kHz. These results confirm that, away from collisions, the cross-drive effects are relatively weak, and motivates a simultaneous SCRP calibration based on the existing individual ECR calibrations (Appendix B).

APPENDIX B: CALIBRATION OF ROTARY TONE FOR SCRP GATE

We describe how we calibrated the rotary tone on the target qubit for the SCRP implementation of a *Z*-parity gate. We calibrated only the amplitude of the rotary tone in this paper; however, our technique is applicable to calibrating the angle as well. We swept 50 amplitude values equally spaced between 0 and a value that corresponds to about $X_{2\pi}$ rotation, and set it to minimize the total estimated error. We defined a cost function for the error as

$$\sum_{Q,R\in\{I,Z\},\ P\in\{Y,Z\}} \|A_{QPR}\|,$$

where A_{QPR} denotes the coefficient of a Pauli *QPR* in the time evolution operator for the gate [discussed later in Eq. (B5)]. In the following, we explain how to estimate the cost function from experimentally available data following and generalizing the HEAT technique [30]. Note that another generalization of HEAT to capture non-Markovian off-resonant errors, not considered in this paper, is proposed in Ref. [53].

1. Echoed CR gate analysis

We first briefly recap HEAT for echoed CR gates with rotary tones to implement a $ZX_{\pi/2}$ gate, following Ref. [30]. HEAT was developed to characterize the time evolution according to a block-diagonal Hamiltonian. In the case of an echoed CR gate, the time evolution unitary operator U over the gate duration t_g can be represented in a block-diagonal Pauli basis as

$$U = \sum_{Q\in\{I,Z\},\ P\in\{I,X,Y,Z\}} A_{QP}\, QP. \tag{B1}$$

HEAT estimates the coefficients A_{QP} from experimentally available statistics. Finally, it reconstructs the coefficients of effective Hamiltonian $\tilde{H}$ by $\tilde{H} = i\log(U)/2t_g$. Here, we omit the last step and use the coefficients of U when using HEAT for the rotary tone calibration.

The block-diagonal form of U means that we have independent subspaces corresponding to initial control states. If the control is in $|0\rangle$, the evolution of the target qubit is described by

$$U_{|0\rangle} = \sum_{P\in\{I,X,Y,Z\}} A_P^{|0\rangle} P = \sum_{P\in\{I,X,Y,Z\}} (A_{IP} + A_{ZP})P,$$

and, if the control is in $|1\rangle$, by

$$U_{|1\rangle} = \sum_{P\in\{I,X,Y,Z\}} A_P^{|1\rangle} P = \sum_{P\in\{I,X,Y,Z\}} (A_{IP} - A_{ZP})P.$$

The point is that A_{IP} and A_{ZP} can be reconstructed from $A_P^{|0\rangle}$ and $A_P^{|1\rangle}$ for any Pauli P in $\{X, Y, Z\}$ since they are related to the Walsh transform.

As $U_{|b\rangle}$ for each $b \in \{0, 1\}$ is a single-qubit rotation, it can be characterized by a generic SU(2) rotation around an axis given by $\hat{n}_b$ with rotation angle θ_b:

$$U_{|b\rangle} = e^{-i(\theta_b/2)\hat{n}_b\cdot(X,Y,Z)},$$

hence, for P in $\{X, Y, Z\}$,

$$A_P^{|b\rangle} = -i\,\hat{n}_{b,P}\sin\left(\frac{\theta_b}{2}\right), \tag{B2}$$

where $\hat{n}_{b,P}$ denotes the P-coordinate value of $\hat{n}_b$.

In particular, we are interested in error terms, i.e., the cases of $P = Y$ or Z. In these cases, the right-hand side of Eq. (B2) can be estimated from experimentally measurable values $\mathrm{tr}(\rho_N^{b,Y} Z)$ and $\mathrm{tr}(\rho_N^{b,Z} Y)$ as follows:

$$\frac{\mathrm{tr}(\rho_N^{b,Y} Z)}{N} \approx -\hat{n}_{b,Y}\sin\theta_b, \quad \frac{\mathrm{tr}(\rho_N^{b,Z} Y)}{N} \approx \hat{n}_{b,Z}\sin\theta_b. \tag{B3}$$

Here $\rho_N^{b,P}$ ($P \in \{Y, Z\}$) is the output state from even N repetitions of the echoed CR pulses with a target refocusing P,

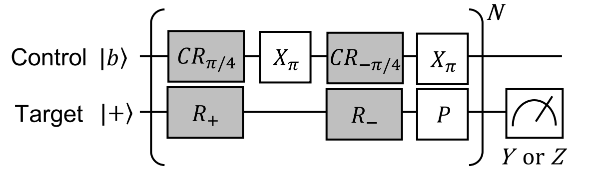

FIG. 6. HEAT pulse sequence for the echoed CR gate [30]. Here, CR represents the entangling cross-resonance pulse, $R_\pm$ represents the rotary tones with opposite amplitudes, P is either Y_π or Z_π, and b represents the initial control state as 0 or 1.

the so-called HEAT sequence, shown in Fig. 6. Moreover, $\mathrm{tr}(\cdot\, Y)$ denotes measuring the target qubit in the Y basis.

From Eqs. (B2) and (B3) with $\theta_b \approx \pm\pi/2$, as we are calibrating the $ZX_{\pi/2}$ gate, we obtain

$$A_Y^{|b\rangle} \approx i\frac{\mathrm{tr}(\rho_N^{b,Y} Z)}{\sqrt{2}N}, \quad A_Z^{|b\rangle} \approx -i\frac{\mathrm{tr}(\rho_N^{b,Z} Y)}{\sqrt{2}N}. \tag{B4}$$

Intuitively, these results can be interpreted as follows: conditional $X_{\pm\pi/2}$ rotation on the target qubit by $ZX_{\pi/2}$ interaction effectively tweaks the rotation axis of Y and Z errors by around $\pi/4$ in the YZ plane, resulting in the scale $1/\sqrt{2}$ for the measurement values.

2. Echoed SCRP gate analysis

In the same way, we consider a model for the echoed SCRP gate with a rotary tone to implement a $ZXI_{\pi/2} + IXZ_{\pi/2}$ gate, which is locally equivalent to the Z-parity gate. Assuming a block-diagonal effective Hamiltonian with Pauli terms only in the form of QPR for $Q, R \in \{I, Z\}$ and $P \in \{I, X, Y, Z\}$, we approximate the unitary evolution as

$$U = \sum_{Q,R\in\{I,Z\},\ P\in\{I,X,Y,Z\}} A_{QPR}\, QPR. \tag{B5}$$

Note that $A_{ZII} = A_{IIZ} = 0$ since they are canceled out by echoing just as $A_{ZI} = 0$ in the echoed CR case [30].

Under the block-diagonal assumption for U, we have four blocks corresponding to the initial control bits $b \in \{00, 01, 10, 11\}$:

$$U_{|b\rangle} = \sum_{P\in\{I,X,Y,Z\}} A_P^{|b\rangle} P, \tag{B6}$$

where

$$\begin{aligned}
A_P^{|00\rangle} &= A_{IPI} + A_{ZPI} + A_{IPZ} + A_{ZPZ},\\
A_P^{|10\rangle} &= A_{IPI} - A_{ZPI} + A_{IPZ} - A_{ZPZ},\\
A_P^{|01\rangle} &= A_{IPI} + A_{ZPI} - A_{IPZ} - A_{ZPZ},\\
A_P^{|11\rangle} &= A_{IPI} - A_{ZPI} - A_{IPZ} + A_{ZPZ}.
\end{aligned}$$

Again, A_{IPI}, A_{ZPI}, A_{IPZ}, and A_{ZPZ} can be reconstructed from $A_P^{|00\rangle}$, $A_P^{|10\rangle}$, $A_P^{|01\rangle}$, and $A_P^{|11\rangle}$ for any Pauli P in $\{X, Y, Z\}$ as they are related with the Walsh transform. Also, similar relations hold as in Eq. (B2) for $b \in \{00, 01, 10, 11\}$.

In contrast, the relationship between experimentally measurable values and the axis of target rotation $\hat{n}_b$ is slightly different, as follows. In the case of $b \in \{01, 10\}$, i.e., $\theta_b \approx 0$,

$$\frac{\mathrm{tr}(\rho_N^{b,Y} Z)}{N} \approx -2\hat{n}_{b,Y}, \quad \frac{\mathrm{tr}(\rho_N^{b,Z} Y)}{N} \approx 2\hat{n}_{b,Z}, \tag{B7}$$

while, in the case when b is 00 or 11, i.e., $\theta_b \approx \pi$ or $-\pi$,

$$\frac{\mathrm{tr}(\rho_N^{b,Y} Y)}{N} \approx -2\hat{n}_{b,Y}, \quad \frac{\mathrm{tr}(\rho_N^{b,Z} Z)}{N} \approx -2\hat{n}_{b,Z}. \tag{B8}$$

Here $\rho_N^{b,P}$ ($P \in \{Y, Z\}$) is the output state of the HEAT sequence for the echoed SCRP gate with input bits b for the control qubits, as shown in Fig. 7. Consequently, for $b \in \{01, 10\}$, we have

$$A_Y^{|b\rangle} \approx i\frac{\mathrm{tr}(\rho_N^{b,Y} Z)}{2N}, \quad A_Z^{|b\rangle} \approx -i\frac{\mathrm{tr}(\rho_N^{b,Z} Y)}{2N}, \tag{B9}$$

which means that we can see Y (Z) rotation errors in the Z (Y) basis as in the case of the CR gate. However, for the case of $b \in \{00, 11\}$, we have

$$A_Y^{|00\rangle} \approx i\frac{\mathrm{tr}(\rho_N^{00,Y} Y)}{2N}, \quad A_Z^{|00\rangle} \approx i\frac{\mathrm{tr}(\rho_N^{00,Z} Z)}{2N}, \tag{B10}$$

$$A_Y^{|11\rangle} \approx -i\frac{\mathrm{tr}(\rho_N^{11,Y} Y)}{2N}, \quad A_Z^{|11\rangle} \approx -i\frac{\mathrm{tr}(\rho_N^{11,Z} Z)}{2N}, \tag{B11}$$

which suggests that we need to measure in the Y (Z) basis in order to see Y (Z) rotation errors, in contrast to the case of the CR gate. The above can be explained by the effect of desirable $ZXI_{\pi/2} + IXZ_{\pi/2}$ interaction on the errors on the target qubit. For example, if the control qubits are in the $|00\rangle$ state ($b = 00$), the desirable interaction rotates the target qubit by π around the X axis, which tweaks the rotation axis of the Y and Z errors by $\pi/2$ in the YZ plane, changing the axes on which the errors appear.

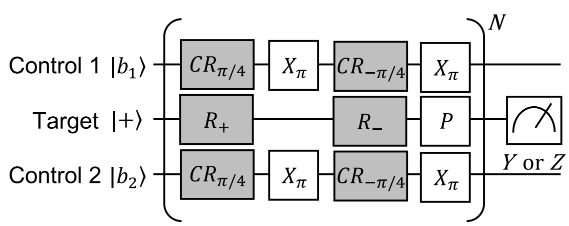

FIG. 7. HEAT pulse sequence for the echoed SCRP gate generalizing Fig. 6. Here, we initialize the control qubits in all four computational states denoted by the bit string $b_1 b_2$.

APPENDIX C: THREE-QUBIT RANDOMIZED BENCHMARKING

We describe how to prepare circuits for three-qubit RB. As we are considering the physical implementation of Z-parity gates, we are interested in RB on qubit triplets on a line (i, j, k). That suggests CNOT gates are natively supported on qubits $\{i, j\}$ and $\{j, k\}$ in a device, but not on qubits $\{i, k\}$. Typically, RB circuits are constructed from sequences of Clifford operations. We construct the circuits in two steps. We first decompose three-qubit Cliffords into basic one- or two-qubit instructions, e.g., Rz (rotation around Z-axis), SX (square root of X) and CNOT for `ibm_auckland`, without considering the connectivity of qubits. Then, if we have any CNOT gates on not-directly-connected qubits $\{i, k\}$, we decompose them further into the sequence of four CNOT gates: CNOT(i, k) into a sequence CNOT(j, k)–CNOT(i, j)–CNOT(j, k)–CNOT(i, j), and similarly for CNOT(k, i).

In the main text, we showed the IRB result on qubits (8, 11, 14) of `ibm_auckland`. We conducted the IRB experiments on two different triplets of qubits, (5, 8, 9) and (13, 14, 16), using the same configurations except for slightly different Clifford lengths: 2, 3, 4, 5, 6, 7, 9, 12, 17, and 25. The results are shown in Figs. 8 and 9, respectively. In the figures, each point represents the average survival rate over 50 sequences for a Clifford length (each error bar indicates the standard deviation of the average) and solid curves represent the fitting curves (their thickness with shaded region indicate 3σ confidence intervals).

APPENDIX D: COHERENCE LIMIT

The *coherence limit* is an estimate of the minimum average error, which can be calculated from the gate length and experimentally measurable noise indicators of each

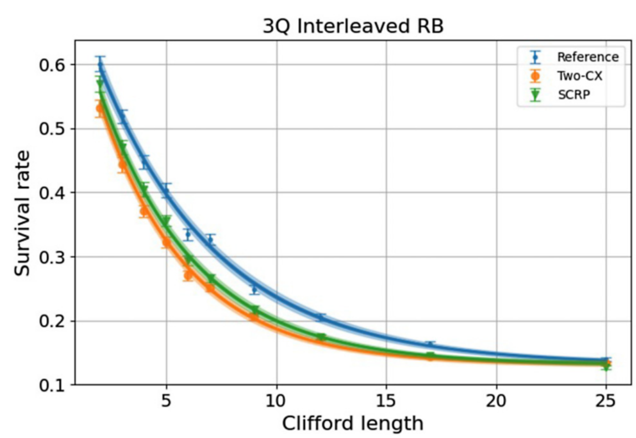

FIG. 8. Interleaved RB comparing two Z-parity gate implementations, the consecutive two CNOT gates (two-CX, orange) and the simultaneous CR drives (SCRP, green) on qubits (5, 8, 9) in `ibm_auckland`. The estimated EPGs are 0.0540 ± 0.0034 (two-CX) and 0.0369 ± 0.0032 (SCRP).

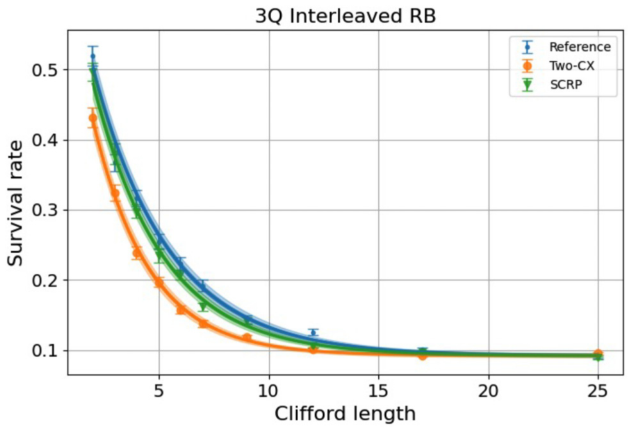

FIG. 9. Interleaved RB comparing two Z-parity gate implementations, the consecutive two CNOT gates (two-CX, orange) and the simultaneous CR drives (SCRP, green) on qubits (13, 14, 16) in `ibm_auckland`. The estimated EPGs are 0.0839 ± 0.0059 (two-CX) and 0.0231 ± 0.0054 (SCRP).

qubit, i.e., energy relaxation (T_1) and dephasing (T_2) times [52,53,67]. It provides a rough lower bound on average gate error in the case when we could implement a gate perfectly on imperfect qubits, assuming only gate-independent single-qubit amplitude damping and dephasing channels.

The coherence limit is formally defined as a special case of the average gate infidelity of a gate U under the above assumption on noise:

$$1 - F_{\mathrm{avg}}(\Lambda(U), U) = \frac{d}{d+1}\left(1 - \frac{\mathrm{tr}[S_\Lambda]}{d^2}\right)$$
$$= \frac{d}{d+1}\left(1 - \prod_{q\in Q}\mathrm{tr}[S_{\Lambda_q}]\right), \quad \text{(D1)}$$

where $\Lambda(U)$ is the quantum channel representing a noisy realization of U, $F_{\mathrm{avg}}(\mathcal{E}, U)$ is the average gate fidelity between a quantum channel $\mathcal{E}$ and a unitary channel U, d is the dimension of the Hilbert space of the n-qubit system (i.e., $d = 2^n$), Q denotes the set of qubits in the system, and S_Λ denotes the Pauli superoperator (or Pauli transfer matrix) representation of the channel Λ. The first equality in Eq. (D1) is obtained from the gate independence of noise. In general, the average gate infidelity and the process (or entanglement) infidelity are related by

$$1 - F_{\mathrm{avg}}(\Lambda(U), U) = \frac{d}{d+1}(1 - F_{\mathrm{pro}}(\Lambda(U), U)).$$

And, for the gate-independent noise channel Λ, we can rewrite those without U since we have $S_{\Lambda(U)} = S_\Lambda S_U$, hence

$$F_{\mathrm{pro}}(\Lambda(U), U) = \frac{\mathrm{tr}[S_U^\dagger S_{\Lambda(U)}]}{d^2} = \frac{\mathrm{tr}[S_\Lambda]}{d^2}.$$

The second equality in Eq. (D1) is obtained from the qubit independence of noise, which allows us to write

$$\mathrm{tr}[S_\Lambda] = \mathrm{tr}\left[\bigotimes_{q\in Q} S_{\Lambda_q}\right] = \prod_{q\in Q}\mathrm{tr}[S_{\Lambda_q}].$$

Recalling the third assumption, that the single-qubit noise Λ_q is an amplitude-phase damping channel, we can explicitly write down the Pauli transfer matrix as

$$S_{\Lambda_q} = \begin{bmatrix} 1 & 0 & 0 & 0 \\ 0 & e^{-t/T_2(q)} & 0 & 0 \\ 0 & 0 & e^{-t/T_2(q)} & 0 \\ 1 - e^{-t/T_1(q)} & 0 & 0 & e^{-t/T_1(q)} \end{bmatrix} \quad \text{(D2)}$$

with the gate length t and the T_1 and T_2 values, $T_1(q)$ and $T_2(q)$, for each $q \in Q$. Consequently, we can compute the coherence limit based on Eqs. (D1) and (D2).

APPENDIX E: DEVICE OVERVIEW

In Tables II and III, we describe the device parameters of the section of `ibm_auckland` we used for the demonstrations in Sec. IV. All values are those reported by the IBM Quantum system as of the day we ran the circuits (August 24, 2023).

TABLE II. Qubit parameters on section of `ibm_auckland` used in this work.

Qubit	Frequency (GHz)	Anharmonicity (MHz)	T_1 (μs)	T_2^{echo} (μs)	EPG (%)	Readout fidelity (%)	$P(0 \mid 1)$	$P(1 \mid 0)$
5	4.993	−344.5	166.2	63.3	0.053	99.1	0.01040	0.00700
8	5.204	−340.7	122.7	73.4	0.021	99.1	0.01220	0.00580
9	5.088	−342.5	76.0	188.5	0.039	96.8	0.05140	0.01280
11	5.055	−342.2	134.8	111.4	0.021	99.4	0.00720	0.00400
13	5.017	−343.7	130.2	25.8	0.028	99.0	0.01460	0.00520
14	5.167	−342.0	159.7	170.3	0.020	99.2	0.00940	0.00580
16	4.970	−343.9	135.0	142.2	0.025	99.4	0.00820	0.00320

$P(1 \mid 0)$ ($P(0 \mid 1)$) is the probability of assigning outcome 1 (0) to a true state $|0\rangle$ ($|1\rangle$).

TABLE III. Two-qubit gate (CX) parameters on section of ibm_auckland used in this work. Shorter CX length suggests the direction, control_target, is native for CR pulses and the reverse direction is accessed by addition of single qubit gates.

Qubit pair	CX length (ns)	EPG (%)
5_8 (8_5)	362.7 (327.1)	0.89
9_8 (8_9)	476.4 (440.9)	0.61
8_11 (11_8)	369.8 (405.3)	0.70
14_11 (11_14)	334.2 (369.8)	0.49
13_14 (14_13)	462.2 (426.7)	0.83
16_14 (14_16)	391.1 (355.6)	0.58

APPENDIX F: DEMONSTRATIONS WITH DYNAMICAL DECOUPLING

We examined how the results of the X-parity measurement experiments discussed in Sec. IV are stable in different qubits in different processors and how they are affected by applying dynamical decoupling (DD) [68–70]. We performed exactly the same X-parity check circuits as described in Sec. IV on these five sets of qubits:

(a) (5, 8, 9, 11, 13, 14, 16) on ibm_auckland,
(b) (0, 1, 2, 4, 6, 7, 10) on ibmq_mumbai,
(c) (16, 19, 20, 22, 24, 25, 26) on ibmq_mumbai,
(d) (92, 102, 101, 103, 105, 104, 111) on ibm_brisbane,
(e) (16, 19, 20, 22, 24, 25, 26) on ibm_sherbrooke,

with and without DD on qubits during their idling time. Note that ibm_auckland and ibmq_mumbai are 27-qubit Falcon processors, while ibm_brisbane and ibm_sherbrooke are 127-qubit Eagle processors. The DD sequence we applied was one of the simplest: Delay(τ)–$X_{+\pi}$–Delay(2τ)–$X_{-\pi}$–Delay(τ) with $\tau \geq 0$.

TABLE IV. Syndrome error rates and data error rates by Z-parity gate implementation in X-parity measurement with and without dynamical decoupling (DD) for different qubits and processors.

Qubits (5, 8, 9, 11, 13, 14, 16) on ibm_auckland						
	Syndrome error (std)	Data error	D1	D2	D3	D4
SCRP	0.088459 (0.001419)	0.095697	0.034948	0.031270	0.017192	0.016798
SCRP w/DD	0.084689 (0.001392)	0.097259	0.039488	0.026717	0.018634	0.017116
Two-CX	0.122878 (0.001639)	0.164109	0.045063	0.034634	0.066089	0.030228
Two-CX w/DD	0.119409 (0.001620)	0.154578	0.043534	0.020895	0.065419	0.035731
Qubits (0, 1, 2, 4, 6, 7, 10) on ibmq_mumbai						
	Syndrome error (std)	Data error	D1	D2	D3	D4
SCRP	0.109272 (0.001548)	0.113695	0.035650	0.023377	0.018956	0.040758
SCRP w/DD	0.106472 (0.001531)	0.113878	0.033192	0.018870	0.022495	0.044358
Two-CX	0.134900 (0.001700)	0.151545	0.037484	0.047234	0.026800	0.049780
Two-CX w/DD	0.109161 (0.001549)	0.129852	0.042086	0.022900	0.025203	0.046937
Qubits (16, 19, 20, 22, 24, 25, 26) on ibmq_mumbai						
	Syndrome error (std)	Data error	D1	D2	D3	D4
SCRP	0.110258 (0.001564)	0.106250	0.020161	0.028778	0.033455	0.028267
SCRP w/DD	0.100983 (0.001504)	0.099725	0.023744	0.025281	0.029089	0.025728
Two-CX	0.154884 (0.001807)	0.153787	0.022800	0.043173	0.051478	0.046066
Two-CX w/DD	0.107333 (0.001545)	0.101486	0.025158	0.024102	0.030133	0.026283
Qubits (92, 102, 101, 103, 105, 104, 111) on ibm_brisbane						
	Syndrome error (std)	Data error	D1	D2	D3	D4
SCRP	0.229439 (0.002088)	0.220552	0.023303	0.163902	0.023650	0.022545
SCRP w/DD	0.211320 (0.002024)	0.198075	0.025081	0.145433	0.017056	0.020922
Two-CX	0.252198 (0.002171)	0.311158	0.027464	0.236027	0.030886	0.043441
Two-CX w/DD	0.225077 (0.002084)	0.313188	0.026216	0.251884	0.031764	0.026294
Qubits (78, 79, 80, 91, 97, 98, 99) on ibm_sherbrooke						
	Syndrome error (std)	Data error	D1	D2	D3	D4
SCRP	0.131761 (0.001677)	0.112402	0.024534	0.047841	0.023861	0.021009
SCRP w/DD	0.117133 (0.001588)	0.102344	0.029244	0.028911	0.024661	0.023788
Two-CX	0.197723 (0.001987)	0.196883	0.026397	0.125797	0.028213	0.029311
Two-CX w/DD	0.138023 (0.001716)	0.132319	0.028781	0.053016	0.030636	0.026558

The results without DD shown in Table IV suggest that the improvements by the SCRP implementation we observed in Sec. IV were universal, regardless of the choice of physical qubits or processors. On the other hand, the improvement percentage (two-CX to SCRP) in the average syndrome error probability depends on qubits, ranging from 9.0% (0.252198 to 0.229439) in `ibm_brisbane` to 33% (0.197723 to 0.131761) in `ibm_sherbrooke`, and it varies even in the same processor, e.g., 19% (0.134900 to 0.109272) for the first qubits (0, 1, 2, 4, 6, 7, 10) and 29% (0.154884 to 0.110258) for the second qubits (16, 19, 20, 22, 24, 25, 26) in `ibmq_mumbai`. It also depends on the time it was executed. The improvements from the other two runs were 26% and 18% for `ibm_brisbane`, 42% and 35% for `ibm_sherbrooke`, and 34% and 20% for the first qubits and 30% and 29% for the second qubits in `ibmq_mumbai`.

Also, as shown in Table IV, the effect of DD depends on the qubits in use and the implementation of the Z-parity gates. For qubits (5, 8, 9, 11, 13, 14, 16) on `ibm_auckland`, there is no improvement in the figures of merit for SCRP implementation, while there is a slight improvement in data error (around 1%) for two-CX implementation. This is not surprising, as DD does not always improve the circuit fidelity, as discussed in Ref. [71]. In contrast, for qubits (16, 19, 20, 22, 24, 25, 26) on `ibm_sherbrooke`, DD improves performance for both SCRP and two-CX implementation. The syndrome error is decreased by around 1.5% for SCRP and 6.0% for two-CX. The data error is decreased by around 1.0% for SCRP and 6.5% for two-CX. DD tends to improve performance more for two-CX implementation than for SCRP. However, even after the application of DD, SCRP implementation still performs better than two-CX implementation. For example, for qubits (5, 8, 9, 11, 13, 14, 16) on `ibm_auckland`, SCRP implementation with DD improved the syndrome error probability from 0.1194 to 0.0847 ($\approx$ 29% improvement) compared with two-CX implementation with DD, while it improved the data error probability from 0.1546 to 0.0973 ($\approx$ 37% improvement).

[1] M. A. Nielsen and I. L. Chuang, Quantum computation and quantum information, Phys. Today **54**, 60 (2001).

[2] A. Y. Kitaev, A. Shen, and M. N. Vyalyi, *Classical and Quantum Computation*, Graduate Studies in Mathematics, vol. 47 (American Mathematical Society, Providence, RI, 2002).

[3] A. Barenco, C. H. Bennett, R. Cleve, D. P. DiVincenzo, N. Margolus, P. Shor, T. Sleator, J. A. Smolin, and H. Weinfurter, Elementary gates for quantum computation, Phys. Rev. A **52**, 3457 (1995).

[4] C. Gardiner and P. Zoller, *Quantum Noise: A Handbook of Markovian and non-Markovian Quantum Stochastic Methods with Applications to Quantum Optics* (Springer Science & Business Media, Berlin, Heidelberg, New York, 2004).

[5] A. A. Clerk, M. H. Devoret, S. M. Girvin, F. Marquardt, and R. J. Schoelkopf, Introduction to quantum noise, measurement, and amplification, Rev. Mod. Phys. **82**, 1155 (2010).

[6] P. Krantz, M. Kjaergaard, F. Yan, T. P. Orlando, S. Gustavsson, and W. D. Oliver, A quantum engineer's guide to superconducting qubits, Appl. Phys. Rev. **6**, 021318 (2019).

[7] D. Maslov, C. Young, D. M. Miller, and G. W. Dueck, in *Proceedings of Design, Automation and Test in Europe* (IEEE, New York, NY, 2005), p. 1208.

[8] D. Maslov, G. W. Dueck, D. M. Miller, and C. Negrevergne, Quantum circuit simplification and level compaction, IEEE Transactions on Computer-Aided Design of Integrated Circuits and Systems **27**, 436 (2008).

[9] V. Kliuchnikov, D. Maslov, and M. Mosca, Asymptotically Optimal Approximation of Single Qubit Unitaries by Clifford and T Circuits Using a Constant Number of Ancillary Qubits, Phys. Rev. Lett. **110**, 190502 (2013).

[10] M. Amy, D. Maslov, and M. Mosca, Polynomial-time T-depth optimization of Clifford+T circuits via matroid partitioning, IEEE Transactions on Computer-Aided Design of Integrated Circuits and Systems **33**, 1476 (2014).

[11] Y. Nam, N. J. Ross, Y. Su, A. M. Childs, and D. Maslov, Automated optimization of large quantum circuits with continuous parameters, Npj Quantum Inf. **4**, 23 (2018).

[12] G. Burkard, D. Loss, D. P. DiVincenzo, and J. A. Smolin, Physical optimization of quantum error correction circuits, Phys. Rev. B **60**, 11404 (1999).

[13] A. Sørensen and K. Mølmer, Entanglement and quantum computation with ions in thermal motion, Phys. Rev. A **62**, 022311 (2000).

[14] A. Fedorov, L. Steffen, M. Baur, M. P. da Silva, and A. Wallraff, Implementation of a Toffoli gate with superconducting circuits, Nature **481**, 170 (2012).

[15] E. A. Martinez, T. Monz, D. Nigg, P. Schindler, and R. Blatt, Compiling quantum algorithms for architectures with multi-qubit gates, New J. Phys. **18**, 063029 (2016).

[16] W. Feng and D.-w. Wang, Quantum Fredkin gate based on synthetic three-body interactions in superconducting circuits, Phys. Rev. A **101**, 062312 (2020).

[17] M. Lu, J.-L. Ville, J. Cohen, A. Petrescu, S. Schreppler, L. Chen, C. Jünger, C. Pelletti, A. Marchenkov, and A. Banerjee *et al.*, Multipartite Entanglement in Rabi-Driven Superconducting Qubits, PRX Quantum **3**, 040322 (2022).

[18] X. Gu, J. Fernández-Pendás, P. Vikstål, T. Abad, C. Warren, A. Bengtsson, G. Tancredi, V. Shumeiko, J. Bylander, and G. Johansson *et al.*, Fast Multiqubit Gates through Simultaneous Two-Qubit Gates, PRX Quantum **2**, 040348 (2021).

[19] C. W. Warren, J. Fernández-Pendás, S. Ahmed, T. Abad, A. Bengtsson, J. Biznárová, K. Debnath, X. Gu, C. Križan, and A. Osman *et al.*, Extensive characterization and implementation of a family of three-qubit gates at the coherence limit, Npj Quantum Inf. **9**, 44 (2023).

[20] Y. Kim, A. Morvan, L. B. Nguyen, R. K. Naik, C. Jünger, L. Chen, J. M. Kreikebaum, D. I. Santiago, and I. Siddiqi, High-fidelity three-qubit *i*Toffoli gate for fixed-frequency superconducting qubits, Nat. Phys. **18**, 783 (2022).

[21] G. S. Paraoanu, Microwave-induced coupling of superconducting qubits, Phys. Rev. B **74**, 140504 (2006).

[22] C. Rigetti and M. Devoret, Fully microwave-tunable universal gates in superconducting qubits with linear couplings and fixed transition frequencies, Phys. Rev. B **81**, 134507 (2010).

[23] V. Tripathi, M. Khezri, and A. N. Korotkov, Operation and intrinsic error budget of a two-qubit cross-resonance gate, Phys. Rev. A **100**, 012301 (2019).

[24] E. Magesan and J. M. Gambetta, Effective Hamiltonian models of the cross-resonance gate, Phys. Rev. A **101**, 052308 (2020).

[25] M. Malekakhlagh, E. Magesan, and D. C. McKay, First-principles analysis of cross-resonance gate operation, Phys. Rev. A **102**, 042605 (2020).

[26] In this term, three-qubit refers to gate (not parity); in fact, a TP gate checks two-qubit parity.

[27] A. D. Córcoles, J. M. Gambetta, J. M. Chow, J. A. Smolin, M. Ware, J. Strand, B. L. Plourde, and M. Steffen, Process verification of two-qubit quantum gates by randomized benchmarking, Phys. Rev. A **87**, 030301 (2013).

[28] S. Sheldon, E. Magesan, J. M. Chow, and J. M. Gambetta, Procedure for systematically tuning up cross-talk in the cross-resonance gate, Phys. Rev. A **93**, 060302 (2016).

[29] P. Jurcevic, A. Javadi-Abhari, L. S. Bishop, I. Lauer, D. F. Bogorin, M. Brink, L. Capelluto, O. Günlük, T. Itoko, and N. Kanazawa *et al.*, Demonstration of quantum volume 64 on a superconducting quantum computing system, Quantum Sci. Technol. **6**, 025020 (2021).

[30] N. Sundaresan, I. Lauer, E. Pritchett, E. Magesan, P. Jurcevic, and J. M. Gambetta, Reducing Unitary and Spectator Errors in Cross Resonance with Optimized Rotary Echoes, PRX Quantum **1**, 020318 (2020).

[31] M. J. Reagor, T. C. Bohdanowicz, D. R. Perez, E. A. Sete, and W. J. Zeng, Hardware optimized parity check gates for superconducting surface codes, arXiv preprint arXiv:2211.06382 (2022).

[32] K. Dodge, Y. Liu, A. R. Klots, B. Cole, A. Shearrow, M. Senatore, S. Zhu, L. B. Ioffe, R. McDermott, and B. L. T. Plourde, Hardware Implementation of Quantum Stabilizers in Superconducting Circuits, Phys. Rev. Lett. **131**, 150602 (2023).

[33] D. M. Greenberger, M. A. Horne, and A. Zeilinger, in *Bell's Theorem, Quantum Theory and Conceptions of the Universe* (Springer, Dordrecht, 1989), p. 69.

[34] D. Bouwmeester, J.-W. Pan, M. Daniell, H. Weinfurter, and A. Zeilinger, Observation of Three-Photon Greenberger-Horne-Zeilinger Entanglement, Phys. Rev. Lett. **82**, 1345 (1999).

[35] P. W. Shor, Scheme for reducing decoherence in quantum computer memory, Phys. Rev. A **52**, R2493 (1995).

[36] A. R. Calderbank and P. W. Shor, Good quantum error-correcting codes exist, Phys. Rev. A **54**, 1098 (1996).

[37] B. M. Terhal, Quantum error correction for quantum memories, Rev. Mod. Phys. **87**, 307 (2015).

[38] S. Lloyd, A potentially realizable quantum computer, Science **261**, 1569 (1993).

[39] D. P. DiVincenzo, D. Bacon, J. Kempe, G. Burkard, and K. B. Whaley, Universal quantum computation with the exchange interaction, Nature **408**, 339 (2000).

[40] The ordering of qubits is (control-0, target, control-1) throughout this paper.

[41] J. R. Schrieffer and P. A. Wolff, Relation between the Anderson and Kondo Hamiltonians, Phys. Rev. **149**, 491 (1966).

[42] S. Bravyi, D. P. DiVincenzo, and D. Loss, Schrieffer–Wolff transformation for quantum many-body systems, Ann. Phys. (N.Y.) **326**, 2793 (2011).

[43] M. Malekakhlagh and E. Magesan, Mitigating off-resonant error in the cross-resonance gate, Phys. Rev. A **105**, 012602 (2022).

[44] M. Malekakhlagh, E. Magesan, and L. C. Govia, Time-dependent Schrieffer-Wolff-Lindblad perturbation theory: Measurement-induced dephasing and second-order Stark shift in dispersive readout, Phys. Rev. A **106**, 052601 (2022).

[45] K. Heya, M. Malekakhlagh, S. Merkel, N. Kanazawa, and E. Pritchett, Floquet analysis of frequency collisions, arXiv preprint arXiv:2302.12816 (2023).

[46] E. Magesan, J. M. Gambetta, B. R. Johnson, C. A. Ryan, J. M. Chow, S. T. Merkel, M. P. Da Silva, G. A. Keefe, M. B. Rothwell, and T. A. Ohki *et al.*, Efficient Measurement of Quantum Gate Error by Interleaved Randomized Benchmarking, Phys. Rev. Lett. **109**, 080505 (2012).

[47] IBM Quantum, https://quantum.ibm.com/ (2021).

[48] C. Chamberland, G. Zhu, T. J. Yoder, J. B. Hertzberg, and A. W. Cross, Topological and Subsystem Codes on Low-Degree Graphs with Flag Qubits, Phys. Rev. X **10**, 011022 (2020).

[49] E. H. Chen, T. J. Yoder, Y. Kim, N. Sundaresan, S. Srinivasan, M. Li, A. D. Córcoles, A. W. Cross, and M. Takita, Calibrated Decoders for Experimental Quantum Error Correction, Phys. Rev. Lett. **128**, 110504 (2022).

[50] N. Sundaresan, T. J. Yoder, Y. Kim, M. Li, E. H. Chen, G. Harper, T. Thorbeck, A. W. Cross, A. D. Córcoles, and M. Takita, Demonstrating multi-round subsystem quantum error correction using matching and maximum likelihood decoders, Nat. Commun. **14**, 2852 (2023).

[51] F. Motzoi, J. M. Gambetta, P. Rebentrost, and F. K. Wilhelm, Simple Pulses for Elimination of Leakage in Weakly Nonlinear Qubits, Phys. Rev. Lett. **103**, 110501 (2009).

[52] J. M. Gambetta, A. D. Córcoles, S. T. Merkel, B. R. Johnson, J. A. Smolin, J. M. Chow, C. A. Ryan, C. Rigetti, S. Poletto, and T. A. Ohki *et al.*, Characterization of Addressability by Simultaneous Randomized Benchmarking, Phys. Rev. Lett. **109**, 240504 (2012).

[53] K. X. Wei, E. Pritchett, D. M. Zajac, D. C. McKay, and S. Merkel, Characterizing non-Markovian off-resonant errors in quantum gates, arXiv preprint arXiv:2302.10881 (2023).

[54] S. B. Bravyi and A. Y. Kitaev, Quantum codes on a lattice with boundary, arXiv preprint arXiv:quant-ph/9811052 (1998).

[55] E. Dennis, A. Kitaev, A. Landahl, and J. Preskill, Topological quantum memory, J. Math. Phys. **43**, 4452 (2002).

[56] A. Kitaev, Anyons in an exactly solved model and beyond, Ann. Phys. (N.Y.) **321**, 2 (2006).

[57] A. G. Fowler, A. M. Stephens, and P. Groszkowski, High-threshold universal quantum computation on the surface code, Phys. Rev. A **80**, 052312 (2009).

[58] A. G. Fowler, M. Mariantoni, J. M. Martinis, and A. N. Cleland, Surface codes: Towards practical large-scale quantum computation, Phys. Rev. A **86**, 032324 (2012).

[59] S. Bravyi, A. W. Cross, J. M. Gambetta, D. Maslov, P. Rall, and T. J. Yoder, High-threshold and low-overhead fault-tolerant quantum memory, arXiv preprint arXiv:2308.07915 (2023).

[60] S. S. Pratapsi and D. Cruz, Improving fidelity of multi-qubit gates using hardware-level pulse parallelization, arXiv preprint arXiv:2312.13350 (2023).

[61] J. B. Hertzberg, E. J. Zhang, S. Rosenblatt, E. Magesan, J. A. Smolin, J.-B. Yau, V. P. Adiga, M. Sandberg, M. Brink, and J. M. Chow *et al.*, Laser-annealing Josephson junctions for yielding scaled-up superconducting quantum processors, Npj Quantum Inf. **7**, 129 (2021).

[62] E. J. Zhang, S. Srinivasan, N. Sundaresan, D. F. Bogorin, Y. Martin, J. B. Hertzberg, J. Timmerwilke, E. J. Pritchett, J.-B. Yau, and C. Wang *et al.*, High-performance superconducting quantum processors via laser annealing of transmon qubits, Sci. Adv. **8**, eabi6690 (2022).

[63] A. Zulehner, A. Paler, and R. Wille, An efficient methodology for mapping quantum circuits to IBM QX architectures, IEEE Transactions on Computer-Aided Design of Integrated Circuits and Systems **38**, 1226 (2018).

[64] G. Li, Y. Ding, and Y. Xie, in *Proceedings of the Twenty-Fourth International Conference on Architectural Support for Programming Languages and Operating Systems* (ACM, New York, NY, 2019), p. 1001.

[65] T. Itoko, R. Raymond, T. Imamichi, and A. Matsuo, Optimization of quantum circuit mapping using gate transformation and commutation, Integration **70**, 43 (2020).

[66] E. Bäumer, V. Tripathi, D. S. Wang, P. Rall, E. H. Chen, S. Majumder, A. Seif, and Z. K. Minev, Efficient long-range entanglement using dynamic circuits, arXiv preprint arXiv:2308.13065 (2023).

[67] T. Abad, J. Fernández-Pendás, A. F. Kockum, and G. Johansson, Universal Fidelity Reduction of Quantum Operations from Weak Dissipation, Phys. Rev. Lett. **129**, 150504 (2022).

[68] L. Viola, E. Knill, and S. Lloyd, Dynamical Decoupling of Open Quantum Systems, Phys. Rev. Lett. **82**, 2417 (1999).

[69] A. M. Souza, G. A. Alvarez, and D. Suter, Robust Dynamical Decoupling for Quantum Computing and Quantum Memory, Phys. Rev. Lett. **106**, 240501 (2011).

[70] D. Suter and G. A. Álvarez, Colloquium: Protecting quantum information against environmental noise, Rev. Mod. Phys. **88**, 041001 (2016).

[71] P. Das, S. Tannu, S. Dangwal, and M. Qureshi, in *Proceedings of MICRO-54: 54th Annual IEEE/ACM International Symposium on Microarchitecture* (ACM, New York, NY, 2021), p. 950.